



Dimethyl sulfide (DMS) climatologies, fluxes, and trends - Part B: Sea-air fluxes

Sankirna D. Joge^{1,2}, Anoop S. Mahajan^{1,*}, Shrivardhan Hulswar¹, Christa A. Marandino³, Martí Galí^{4,5}, Thomas G. Bell⁶, Mingxi Yang⁶ and Rafel Simo⁴

5 ¹Indian Institute of Tropical Meteorology, Pune, India

²Savitribai Phule Pune University, Pune, India

³Research Division 2-Biogeochemistry, GEOMAR Helmholtz Centre for Ocean Research Kiel, Kiel, Germany

⁴Institut de Ciències del Mar (CSIC), Barcelona, Catalonia, Spain

⁵ Barcelona Supercomputing Center (BSC), Barcelona, Spain

10 ⁶Plymouth Marine Laboratory (PML), Plymouth, UK

*Correspondence to: Anoop S. Mahajan (anoop@tropmet.res.in)

Abstract. Dimethyl sulfide (DMS) significantly contributes to cloud condensation nuclei (CCN) formation in the marine environment. DMS is ventilated from the ocean to the atmosphere, and in most models, this flux is calculated using seawater DMS concentrations and a sea-air flux parameterization. Here, climatological seawater DMS concentrations from interpolation and parameterization techniques are passed through seven flux parameterizations to estimate the DMS flux. The seasonal means of calculated fluxes are compared to identify differences in absolute values and spatial distribution, which show large differences depending on the flux parameterization used. In situ flux observations were used to validate the estimated fluxes from all seven parameterizations. Even though we see a correlation between the estimated and observed values, all methods underestimate the fluxes in the higher range ($>20 \mu\text{mol m}^{-2} \text{d}^{-1}$) and overestimate the fluxes in the lower range ($< 20 \mu\text{mol m}^{-2} \text{d}^{-1}$). The estimated uncertainty in DMS fluxes is driven by the uncertainty in seawater DMS concentrations in some regions but by the choice of flux parameterization in others. We show that the resultant flux is hence highly sensitive to both and suggest that there needs to be an improvement in the estimation methods of global seawater DMS concentration and sea-air fluxes for accurately modeling the effect of DMS on the atmosphere.

15
20

1 Introduction

25 Dimethyl sulfide (DMS) is a marine-derived compound responsible for influencing climate change, which is obtained from the phytoplankton life cycle through the enzymatic cleavage of dimethylsulfoniopropionate (DMSP) (Andreae and Crutzen, 1997; Charlson et al., 1987; Simó, 2001). The DMS emitted from the surface ocean is responsible for up to 70 % of the natural sulfur emissions into the global atmosphere (Andreae and Raemdonck, 1983; Carpenter et al., 2012). Due to its effect on



30 incoming solar radiation, this biogeochemical cycle plays a vital role in the Earth's climate system (Andreae and Crutzen, 1997; Charlson et al., 1987).

The emission of DMS occurs due to differences in concentrations of DMS in the seawater and the atmosphere. The sea-air gas transfer is a complex process, with the wind proven to be one of the most influencing factors (Jähne et al., 1979). Hence, the sea-air gas transfer is parameterized as a function of wind speed. Kettle and Andreae (2000) ~~carried out a comparative study between~~ three parametrizations viz., Liss & Merlivat (1986), Wanninkhof (1992), and Erickson (1993). They concluded that
 35 a significant uncertainty in the flux parameterizations leads to uncertainties in estimating the global DMS flux. Furthermore, different datasets for wind speed, sea surface temperature (SST), and sea surface DMS concentration resulted in relatively small variations in these calculated fluxes ($\leq 25\%$) (Kettle and Andreae, 2000).

Here, we compare global sea-air DMS fluxes derived using seven different gas transfer velocity parameterizations using wind speed and SST. The comparison is conducted using different seawater DMS estimations to identify whether the uncertainty in
 40 the emissions is larger because of the uncertainty in seawater DMS concentrations or the flux parameterization. We use one interpolation-based seawater DMS concentration climatology ((Hulswar et al., 2022), hereafter referred to as H22) and two parameterization-based seawater DMS climatologies (Galí et al. (2018), hereafter referred to as G18 and Wang et al. (2020), hereafter referred to as W20. A comparison between the three seawater DMS climatologies is presented in the sister paper (Joge et al., referred to as Joge: Part A). Here, we inter-compared the DMS fluxes estimated using seven sea-air flux
 45 parameterizations and in situ DMS fluxes and identified the drivers of their uncertainties.

2 Data and methodology

For DMS flux calculation, seven parametrization schemes (LM86 (Liss and Merlivat, 1986), E93 (Erickson, 1993), N00a, N00b (Nightingale et al., 2000), Ho06 (Ho et al., 2006), GM12 (Goddijn-Murphy et al., 2012), W14 (Wanninkhof, 2014)) are used with the seawater DMS climatological data of H22, G18, and W20 (please check Joge: Part A for a comparison between
 50 the seawater DMS estimations). Each flux parametrization scheme uses wind speed, and some also use SST to estimate the DMS sea-air flux. Wind speed and SST were obtained from the National Centers for Environmental Prediction (NCEP; <https://psl.noaa.gov/data/gridded/index.html>) (Kalnay et al., 1996) and Centennial in situ Observation-Based Estimates (COBE; <https://psl.noaa.gov/data/gridded/data.cobe.html>) (Ishii et al., 2005), respectively, for the years from 1948 to 2022, and then monthly averaged to calculate the fluxes.

55 In general, all the parameterizations we compare in this study depend on wind speed (u) and the Schmidt number (Sc), which depends on temperature (T). The Schmidt number (Sc) is a dimensionless number defined as the ratio of momentum diffusivity (ν) and mass diffusivity (D), i.e., $Sc = \nu/D$ (Liss and Merlivat, 1986). The DMS sea-air flux is determined by using a bulk flux equation $F = k(C_w - C_a/H)$ where F is the calculated DMS flux, k is the gas transfer velocity, and C_w and C_a are the concentrations of the DMS in the seawater and the atmosphere adjacent to the seawater respectively (Wanninkhof, 2014). H
 60 is Henry's law solubility for DMS in seawater, which varies with temperature, which is given as $\ln H = -3547/T + 12.64$ (Dacey

and Wakeham, 1984). Here, C_a and C_w are measured in situ, while k depends on wind speed. C_w is several orders of magnitude higher than C_a ; hence C_a/H is often ignored (Yan et al., 2023). The seven parameterizations discussed give estimates of the k and Sc values.

As wind is one of the most influential factors affecting gas transfer, most parameterizations have established different wind speed regimes for which different equations estimate the k values. The gas transfer velocity k results from the waterside transfer velocity (k_w) and airside transfer velocity (k_a). For the rarely soluble gas, airside resistance is usually small and neglected, but DMS solubility increases with a decrease in temperature, and hence, air resistance becomes important (Lana et al., 2011; Marandino et al., 2009; Omori et al., 2017). Most parameterizations agree that at wind speeds less than 3.6 m s^{-1} , the surface is generally smooth with few waves, known as the ‘smooth surface regime.’ When the wind speed is above 3.6 m s^{-1} but less than 13 m s^{-1} , it is ‘rough surface regime,’ and more waves are observed, enhancing the gas transfer. Above 13 m s^{-1} is known as the ‘breaking wave regime,’ where bubbles are formed along with the waves, significantly increasing the flux as evident from the Heidelberg circular wind tunnel experiments (Jähne et al., 1984; Jahne et al., 1979; Liss and Merlivat, 1986). The different flux parameterizations estimate the k value in those different wind regimes ($u \leq 3.6$: smooth surface regime, $3.6 < u \leq 13$: rough surface regime, $u > 13$: breaking wave regime), and these wind regimes are also dependent on the Schmidt number (Sc) for each parametrization, where Schmidt number depends on temperature (T).

2.1 Flux parameterization methods

2.1.1 LM86 Flux Parametrization

LM86 formulated the following equations for the three wind regimes, which are defined below following the results of the Heidelberg experiments (Jahne et al., 1979; Jähne et al., 1984) :

$$k_{lm86} = 0.17 \times (600/Sc)^{2/3} \times u \quad (u \leq 3.6) \quad (1)$$

$$k_{lm86} = (600/Sc)^{1/3} \times (2.85 \times u - 10.26) + 0.61 \times (600/Sc)^{2/3} \quad (3.6 < u \leq 13) \quad (2)$$

$$k_{lm86} = (600/Sc)^{1/3} \times (5.9 \times u - 49.91) + 0.61 \times (600/Sc)^{2/3} \quad (u > 13) \quad (3)$$

Here, u is the wind speed in m s^{-1} at 10 m above the sea surface. The Sc is based on the work carried out by Saltzman *et al.* (1993) and the references therein for the temperature range from 5°C to 30°C using:

$$Sc = 2674 - (147.12 \times SST) + (3.726 \times SST^2) - (0.038 \times SST^3) \quad (4)$$

2.1.2 E93 Flux Parameterization

Erickson (1993) assumed that the sea surface is a mixture of a low-turbulence area (non-whitecap) and a high-turbulence area (whitecap). The gas transfer velocities are obtained from the radon outgassing data obtained during the expedition of Transient Tracers in the Ocean (TTO) and Geochemical Ocean Sections Study (GEOSECS) (Monahan and Spillane, 1984; Kettle and



90 Andreae, 2000). The gas transfer velocities for other species are calculated using the following conversion formula based on wind speed ranges:

$$k_{e93} = k_{Rn} \times \left(Sc / Sc_{Rn} \right)^{-2/3} \quad (u < 3.6) \quad (5)$$

$$k_{e93} = k_{Rn} \times \left(Sc / Sc_{Rn} \right)^{-1/3} \quad (u \geq 3.6) \quad (6)$$

Here, k_{Rn} (Monahan and Spillane, 1984) and Sc_{Rn} are the gas transfer velocity and Schmidt number for radon, respectively, which are given as follows:

$$95 \quad k_{Rn} = 2.3 + 1.25 \times 10^{-3} \times u^3 \quad (u \text{ in m d}^{-1}) \quad (7)$$

$$Sc_{Rn} = 3147.3 - 201.9 \times SST + 5.5 \times SST^2 - 0.055 \times SST^3 \quad (8)$$

2.1.3 N00a and N00b Flux Parametrization

Dual tracer methods (Watson et al., 1991) involving the measurements of sulfur hexafluoride SF₆ and 3-Helium (³He) were also used to estimate k (Watson et al., 1991). Nightingale et al. (2000) describe the ideal dual tracer combination as the one with one of the tracers being non-volatile, allowing dilution and dispersion corrections to be applied to the volatile tracer to minimize errors while estimating k . Due to the absence of such an ideal marine tracer, Nightingale et al. (2000) introduced a novel method of adding metabolically inactive bacterial spores of *Bacillus globigii* var. *Niger* as a conservative tracer to study the gas exchange in the North Sea (Watson et al., 1991; Nightingale et al., 2000) along with SF₆ and ³He dual tracer for comparison. Combining data from other studies in George's Bank (Wanninkhof et al., 1993) and the West Florida shelf (Wanninkhof et al., 1997) with the North Sea data, the N00a parameterization coefficient was given as

$$105 \quad k_{n00a} = (0.222 \times u^2 + 0.333 \times u) \times \left(Sc / 600 \right)^{-0.5} \quad (9)$$

However, this study exclusively had data from the Northern Atlantic region. Coale et al. (1996) reported k values by using the dual tracer (SF₆/³He) in the equatorial Pacific Ocean, which was then used to upgrade the N00a parameterization to N00b; the upgraded parameterization is given as

$$110 \quad k_{N00b} = (0.222 \times u^2 \times \text{shape parameter} + 0.333 \times u) \times \left(Sc / 600 \right)^{-0.5} \quad (10)$$

Here, the *shape parameter* is used to describe variations in wind speed using Weibull Distribution.

2.1.4 Ho06 Flux Parameterization



115 Ho et al. (2006) applied the dual tracer technique to measure the gas transfer velocity with the wind speed ranging from 7–16 m s⁻¹. This was done during the Surface Ocean Lower Atmosphere Study (SOLAS) Air-Sea Gas Exchange (SAGE) campaign. The estimation of Ho06 was derived from the SAGE data, and the gas transfer coefficient is given as,

$$k_{ho06} = (0.266 \pm 0.019) \times u^2 \quad (11)$$

2.1.5 GM12 Flux Parametrization

120 Goddijn-Murphy et al. (Goddijn-Murphy et al., 2012) argued that since the wind does not directly affect the gas transfer, it is the turbulence caused due to wind that helps to form bubbles, which increases gas transfer. Hence, the sea-surface roughness is a better parameter to quantify gas transfer. This study used satellite altimetry data to understand the sea surface roughness and measured DMS gas transfer velocity using the eddy covariance flux determination from eight cruises. This resulted in the new GM12 parameterization, which gives gas transfer velocity given as,

$$k_{gm12} = 2.1 \times u - 2.8 \quad (12)$$

125 2.1.6 W14 Flux Parametrization

Wanninkhof (1992) used the radiocarbon ¹⁴C data from the Red Sea (Cember, 1989) to understand the CO₂ gas exchange rates. Based on this, the parametrization was developed using *Sc* number related to the work carried out by Saltzman *et al.* (1993) with the temperature range between 18° C to 25° C. Further, with the help of better quantification of global wind fields and using data with a broader temperature range (-2° C to 40° C), the parametrization developed in 1992 is being upgraded using
130 revised global ocean ¹⁴C inventories and improved wind speed product. This new parametrization technique is known as W14, which gives a gas transfer velocity equation:

$$k_{w14} = 0.251 \times u^2 \times \left(\frac{Sc_{w14}}{660} \right)^{-0.5} \quad (13)$$

Here:

$$Sc_{w14} = 2855.7 - 177.63 \times SST + 6.0438 \times SST^2 - 0.11645 \times SST^3 + 0.00094743 \times SST^4 \quad (14)$$

135 2.2 Estimation of uncertainties

The total uncertainty in DMS fluxes (σ_{total}) is calculated using the standard deviations in seawater DMS concentration (σ_{DMS}), coefficient of parameterization (σ_k), and wind speed (σ_{wind}):

$$\sigma_{total} = \sqrt{\sigma_{DMS}^2 + \sigma_k^2 + \sigma_{wind}^2} \quad (15)$$

140 The flux due to σ_{DMS} is computed for each pixel using the standard deviation between the seawater DMS concentrations of H22, W20, and G18, which is then passed through the N00b parametrization. The flux due to σ_k is calculated by calculating the standard deviation between the coefficients of all seven flux parameterizations. The flux due to σ_{wind} is computed using



standard deviation between monthly global wind data from the different sources (NCEP Reanalysis 1, NCEP/DOE Reanalysis 2, ECMWF Reanalysis v5 (ERA5)), and then it is passed through N00b parameterization. Here, N00b is chosen as it has been used **historically in previous studies** (Simó and Dachs, 2002; Lana et al., 2011; Hulswar et al., 2022; McNabb and Tortell, 2022; Zhang et al., 2021; Zhao et al., 2003) for the calculation of fluxes. Finally, σ_{total} is obtained using Eq.(15).
145

3 Results and discussion

3.1 Salient features and seasonal variations

We estimated the seasonal DMS flux using seven different parameterizations and the global seawater DMS data of H22 (Fig.1), G18 (Fig.S1), and W20 (Fig.S2) climatologies to study the geographical and seasonal variations and the differences between the parameterizations.
150

Overall, the fluxes estimated using all seven parameterizations follow the seawater DMS concentration distribution, with higher values in the southern/northern hemispheres during their respective summers (Fig.1). Elevated levels are also seen in the Indian, Atlantic, and Pacific Oceans in the extra-tropical regions, where elevated wind speed causes higher sea-air fluxes. While the geographical patterns are similar, there is a large difference in the absolute values **between** the different parameterizations. When using the G18 or W20 seawater DMS concentrations, the emissions show a similar difference **between** the different parameterizations, although the absolute values are lower (Fig.S1 and S2).
155

In December-January-February (DJF), E93 shows a maximum DMS flux of $45.82 \mu\text{mol m}^{-2} \text{d}^{-1}$ in the Weddell Sea region, where the maximum DMS concentration of 18.67 nM is also observed in H22 (Joge: Part A). For E93, the flux is more uniformly distributed across the Southern Ocean as compared to the other parameterizations (Fig.1). The other parameterizations also show elevated values in the Southern Ocean, although the range depends on the parameterization used. For example, the E93 parameterization results in the highest values, exceeding $20 \mu\text{mol m}^{-2} \text{d}^{-1}$ throughout the Southern Ocean, while the LM86 parameterization results in peak values less than $10 \mu\text{mol m}^{-2} \text{d}^{-1}$. Further north, in other ocean basins such as the Indian Ocean Ho06, and N00b predict relatively higher fluxes than E93.
160

During March-April-May (MAM), most parameterizations **predict** elevated fluxes in the North Atlantic Ocean, Caribbean Sea, Baltic Sea, and North Sea, with the DMS flux ranging from 8.71 to $18.73 \mu\text{mol m}^{-2} \text{d}^{-1}$ using the H22 seawater DMS concentrations. Higher fluxes are also observed on the western coast of the American continent and in the coastal regions of Africa. The gyres in the equatorial Pacific and Indian Oceans also show higher fluxes, although the Northern Atlantic Ocean has higher fluxes than the other ocean basins. Although all the parameterizations show higher values in the northern hemisphere, E93 shows the **relatively** highest fluxes, and the LM86 parameterization shows the lowest fluxes. In a similar manner, N00b shows high flux values ($13.8 \mu\text{mol m}^{-2} \text{d}^{-1}$) compared to N00a ($11.33 \mu\text{mol m}^{-2} \text{d}^{-1}$) in the Caribbean Sea, probably due to the wind correction factor in N00b parametrization.
165

June-July-August (JJA) period shows high values in the upwelling regions off the continental coasts and the equatorial Indian Ocean and Pacific Ocean. During this period, the geographical variation strongly depends on the parameterization chosen. For
170



175 example, the E93 parameterization mainly shows peaks in the Arctic Ocean and the northern boundaries of the other ocean basins. However, others show peaks in the equatorial oceans in addition to the northern latitudes. This difference in variation is driven by the different sensitivity of the parameterizations to winds.

Flux values start increasing in the Southern Ocean during September-October-November (SON). The flux value estimated by Ho06 were the highest during this period ($18.40 \mu\text{mol m}^{-2} \text{d}^{-1}$) in the south Atlantic Ocean near the coast of South Africa, although the other parameterizations also show an increase in the Southern Ocean except for LM86. A distinct hotspot is also
180 seen in the Indian Ocean region in all estimations such as Ho06 followed by N00a ($13.77 \mu\text{mol m}^{-2} \text{d}^{-1}$), N00b ($16.75 \mu\text{mol m}^{-2} \text{d}^{-1}$), GM12 ($11.97 \mu\text{mol m}^{-2} \text{d}^{-1}$), and W14 ($13.84 \mu\text{mol m}^{-2} \text{d}^{-1}$), while LM86 estimated the least ($10.66 \mu\text{mol m}^{-2} \text{d}^{-1}$) in the Indian ocean region.

3.2 Differences

We calculated the seasonal differences between all the flux parameterizations with respect to the N00b (Fig.2), which is still
185 one of the most commonly used parameterizations (Lana et al., 2011; Hulswar et al., 2022). Annually, the largest positive difference is seen in the LM86 parameterization, which consistently displays lower values than the N00b parameterization. The largest negative differences in the polar regions are observed in the E93 parameterization, which shows that higher values are calculated at those regions than the N00b parameterization. Although Ho06 also shows large negative differences in the polar regions, large positive differences are observed in the mid-latitude and coastal regions. These differences can be as much as
190 100 % in certain regions, showing that the choice of parameterization plays a crucial role in the DMS flux estimates.

The largest positive differences ($8.10 \mu\text{mol m}^{-2} \text{d}^{-1}$ in DJF, $5.15 \mu\text{mol m}^{-2} \text{d}^{-1}$ in MAM, $14.29 \mu\text{mol m}^{-2} \text{d}^{-1}$ in JJA and $6.11 \mu\text{mol m}^{-2} \text{d}^{-1}$ in SON) are observed in N00b-LM86, while the largest negative differences ($-38.93 \mu\text{mol m}^{-2} \text{d}^{-1}$ in DJF, $-14.48 \mu\text{mol m}^{-2} \text{d}^{-1}$ in MAM, $-11.32 \mu\text{mol m}^{-2} \text{d}^{-1}$ in JJA and $-10.61 \mu\text{mol m}^{-2} \text{d}^{-1}$ in SON) are with E93. This large negative difference is driven by the differences in the high latitude regions where N00b does not show significant peaks, for example, in the
195 Southern Ocean (Fig.1). In the mid-latitude and the equatorial regions, significant peaks are observed in N00b estimations and hence N00b-E93 shows largest positive difference of $8.18 \mu\text{mol m}^{-2} \text{d}^{-1}$ in DJF, $6.32 \mu\text{mol m}^{-2} \text{d}^{-1}$ in MAM both in the Caribbean Sea, $18.45 \mu\text{mol m}^{-2} \text{d}^{-1}$ in JJA in the Indian Ocean near the coast of Somalia, and $6.81 \mu\text{mol m}^{-2} \text{d}^{-1}$ in SON in the Indian Ocean near Mauritius.

Although N00b is upgraded from N00a parameterization, there is no negative difference between the two parametrizations
200 (Fig.2), which indicates that N00b estimates higher flux values than N00a everywhere (Fig.1). The maximum positive differences between the two range from $2.47 \mu\text{mol m}^{-2} \text{d}^{-1}$ in MAM in the Caribbean Sea to $6.12 \mu\text{mol m}^{-2} \text{d}^{-1}$ in JJA in the Indian Ocean near Somalia. The differences between N00b and Ho06 are primarily negative and range from $-3.92 \mu\text{mol m}^{-2} \text{d}^{-1}$ to $-10.59 \mu\text{mol m}^{-2} \text{d}^{-1}$ in the Southern Ocean, while positive differences are lower than N00b-N00a and the range is from 1.5 to $2.37 \mu\text{mol m}^{-2} \text{d}^{-1}$.

205 The difference between N00b and GM12 is positive. Seasonally, the maximum positive difference is $16.17 \mu\text{mol m}^{-2} \text{d}^{-1}$ in JJA in the Indian Ocean near Somalia, $4.37 \mu\text{mol m}^{-2} \text{d}^{-1}$ in MAM, and $5.93 \mu\text{mol m}^{-2} \text{d}^{-1}$ in DJF in the Caribbean Sea, 4.94



210 $\mu\text{mol m}^{-2} \text{d}^{-1}$ in SON in the Indian Ocean near Mauritius. Similarly, in the case of N00b-W14, significant positive differences are observed. The maximum difference of $4.52 \mu\text{mol m}^{-2} \text{d}^{-1}$ in JJA in the Indian Ocean near Somalia, $2.59 \mu\text{mol m}^{-2} \text{d}^{-1}$ in MAM in the North Sea, $4.12 \mu\text{mol m}^{-2} \text{d}^{-1}$ in DJF in the Ross Sea and $2.93 \mu\text{mol m}^{-2} \text{d}^{-1}$ in SON in the Indian Ocean near Mauritius can be seen from Figure 2. Flux estimated with W14 parameterization shows positive differences with N00b with minimum difference of $0.04 \mu\text{mol m}^{-2} \text{d}^{-1}$ and maximum difference of $4.52 \mu\text{mol m}^{-2} \text{d}^{-1}$.

3.3 Drivers in flux uncertainties

As explained in the methods section, the total uncertainty in DMS fluxes is **driven by** the uncertainty in the seawater DMS concentrations, parameterization, and wind speed.

215 Figure S3 shows the standard deviation in the DMS flux calculated using the standard deviation between climatological seawater DMS concentrations (σ_{DMS}) of G18, W20, and H22. Here, the sea-air parameterization is kept constant to isolate the effect of the change due to seawater DMS concentrations (**we use N00b for this calculation**). The monthly climatological wind speed data (NCEP reanalysis 1) is used for the flux estimation. In DJF, the maximum standard deviation of $34.64 \mu\text{mol m}^{-2} \text{d}^{-1}$ is **observed** in January near the coast of Namibia in the South Atlantic Ocean, while high values of up to $28.76 \mu\text{mol m}^{-2} \text{d}^{-1}$ are observed near the coast of South Africa of South Atlantic Ocean. In JJA, a maximum standard deviation of $23.87 \mu\text{mol m}^{-2} \text{d}^{-1}$ is observed near the coast of Oman in the Arabian Sea in July, while high values up to $21.86 \mu\text{mol m}^{-2} \text{d}^{-1}$ are seen around the same region in August. During the MAM season, the maximum σ_{DMS} ($20.55 \mu\text{mol m}^{-2} \text{d}^{-1}$) is observed **May** near the Gulf of Kutch **of Arabian Sea**, while in SON, the maximum σ_{DMS} ($18.40 \mu\text{mol m}^{-2} \text{d}^{-1}$) is observed in the South Atlantic Ocean near the coast of Namibia. Overall, the largest standard deviation in σ_{DMS} is in the Southern Ocean, where the DMS concentrations are the largest.

225 Figure S4 shows the standard deviation in the DMS flux due to the different flux parameterizations (σ_k). Here, we keep the seawater DMS concentrations constant (H22), and monthly climatological wind speed data of NCEP reanalysis 1 is used. In DJF season, large σ_k values ranging between 6.99 to $21.70 \mu\text{mol m}^{-2} \text{d}^{-1}$ are **observed** in the regions close to the Antarctic Peninsula. In JJA, large values between 5.75 to $8.86 \mu\text{mol m}^{-2} \text{d}^{-1}$ are observed in the Somali basin of the Indian Ocean. In MAM, this peak range is from 3.17 to $9.12 \mu\text{mol m}^{-2} \text{d}^{-1}$ in the South Atlantic Ocean near Congo Canyon, the Baltic Sea, and the Prince of Wales near the Gulf of Alaska. In SON, the peak σ_k ranges between 2.93 to $10.43 \mu\text{mol m}^{-2} \text{d}^{-1}$ in the Somalian basin, Bay of Bengal, and the Antarctic region. Annually averaged, the maximum σ_k value of $5.35 \mu\text{mol m}^{-2} \text{d}^{-1}$ is obtained around Antarctica in the Southern Ocean.

235 **Further, the standard deviation in the DMS flux is estimated again with the standard deviation in wind speed (σ_{wind}), which is obtained through the standard deviation between monthly wind speed data from different sources (NCEP reanalysis 1, NCEP/DOE reanalysis 2, ERA5), with the seawater DMS concentration of H22 and a flux parameterization equation (N00b).** The area weighted global mean flux standard deviation due to σ_{wind} was much lower than the area weighted global mean flux std due to σ_{DMS} and σ_k on monthly and annual scales (Table 1). The maximum annual average of $2.62 \mu\text{mol m}^{-2} \text{d}^{-1}$ due to



σ_{wind} is obtained near the Cape Adare of Antarctica. This shows that the total standard deviation of the sea-air DMS flux (σ_{total} is calculated using Eq.(15)) is dominated by σ_{DMS} and σ_k , with σ_{wind} playing a minor role in the total flux uncertainty (Table 1). The climatological monthly and annual σ_{total} are shown in Figure 3. In DJF, the maximum σ_{total} observed is $22.66 \mu\text{mol m}^{-2} \text{d}^{-1}$ in the regions close to the Antarctic Peninsula. In JJA, the maximum σ_{total} was $24.60 \mu\text{mol m}^{-2} \text{d}^{-1}$ near coastal Oman in the Arabian Sea. In MAM, the higher values of σ_{total} range between 12.68 to $17.17 \mu\text{mol m}^{-2} \text{d}^{-1}$, with the highest value in the North Atlantic Ocean near Western Sahara. In SON, the highest σ_{total} is $16.47 \mu\text{mol m}^{-2} \text{d}^{-1}$, in the South Atlantic Ocean near the west coast of South Africa. At an annual scale, the maximum total deviation is $8.55 \mu\text{mol m}^{-2} \text{d}^{-1}$, is observed in the North Atlantic ocean near the coast of Mauritania, although the Southern Ocean also shows significant values of σ_{total} along with coastal regions of South America and Africa.

As mentioned above, the σ_{total} of DMS flux is dominated by σ_{DMS} and σ_k , with σ_{wind} having a minor contribution (Table 1). In Figure 3, the regions where the σ_{total} is dominated by the variation in seawater DMS concentrations, i.e., $\sigma_{DMS} > \sigma_k$, are indicated by red dots. The regions where the red dots are absent are the ones where the dominant contribution to σ_{total} is due to σ_k . It is observed that σ_{total} in oligotrophic oceans and most of coastal areas are dominated by σ_{DMS} . Annually, the σ_{total} in the Southern Ocean is dominated by σ_{DMS} , but the coastal area of Antarctica is dominated by σ_k . Table 1 also shows the total DMS_{sulfur} flux to the atmosphere according to each month and annually averaged. For most of the year, the total flux from regions where σ_{DMS} is greater than σ_k is larger. Indeed, the total annual flux of DMS_{sulfur} to the atmosphere is estimated as 22.08 Tg , of which 17.16 Tg is contributed by areas where $\sigma_k < \sigma_{DMS}$. This indicates that on an annual scale, the uncertainty in DMS_{sulfur} emissions is dominated by seawater DMS concentration. However, from Figure 3, the choice of the flux parametrization also contributes a significant amount of uncertainty in coastal areas of Antarctica, which can be observed in November, December, January, and February. Overall, the choice of seawater DMS estimation method has larger influence on sea-air DMS flux than the choice of flux parameterization (Bhatti et al., 2023).

3.4 Comparison with in situ observations

In situ DMS flux data measured by eddy covariance or gradient flux techniques was obtained from various studies carried out over the global oceans (Table S1). These were compared with the co-located DMS flux data estimated from different parameterizations using the H22 (Fig.4), G18 (Fig.S5), and W20 (Fig.S6). In this analysis, the in situ DMS flux data is monthly binned to $1^\circ \times 1^\circ$ spatial resolution as the estimated DMS flux climatologies are also at the same resolution, and then ordinary least square regression is applied. For reference, raw in situ DMS flux points are shown in the background (Fig.4, S5 and S6). All flux estimates using either of the DMS seawater climatologies, with any of the flux parameterizations, struggle to match the observations.

In most cases, the flux estimations in the lower range ($< 20 \mu\text{mol m}^{-2} \text{d}^{-1}$) are overestimated, while the values are underestimated in the higher range ($> 20 \mu\text{mol m}^{-2} \text{d}^{-1}$). Indeed, in all the cases, a positive intercept in the linear regressions shows that the emissions are overestimated at lower flux values. This would indicate a constant background flux in the estimated emissions,



which would overestimate the total $\text{DMS}_{\text{sulfur}}$ flux to the atmosphere. In contrast, the fact that the flux estimates do not reproduce the higher DMS fluxes indicates that high emission scenarios, which would contribute strongly to new particle formation and growth, are underestimated by the emission estimations. It should be noted that we use monthly seawater DMS concentration fields as input. Hence, a difference between the observations and estimations is expected, **but a consistent**
275 **difference in lower and higher ranges points to emissions being overestimated/underestimated in models.** The best match in the lower range is found when using the W20 seawater DMS estimations (Fig.S6), although the slope is consistently lower than 0.33, and the intercept is higher than 2.17 for all the flux parameterizations ($R^2 < 0.32$ for all the parameterizations). Both H22 and W20 perform **relatively** better than G18, but none of the correlation coefficients are found to be significant, and all the flux parametrization methods fail to reproduce the in situ DMS flux values, particularly the high values of fluxes. (Fig.4,
280 S5 and S6).

4 Conclusions

The sea-air DMS flux was estimated using different seawater DMS climatologies (see Joge: Part A), wind, and SST as input to seven different flux parameterizations. All the flux estimations show a similar seasonal variation, with peaks in the summers
285 of each hemisphere. However, there were large geographical and absolute flux differences **between** the different estimations, showing that the $\text{DMS}_{\text{sulfur}}$ flux to the atmosphere is sensitive to the chosen seawater DMS fields and the chosen flux parameterization. The total uncertainty in flux estimation is dominated by the uncertainty in seawater DMS concentrations and the choice of flux parametrization, while the effect on the total uncertainty due to ~~standard deviation between~~ the different sources of wind data is not as **significant**; however, this might not be true when comparing to in situ fluxes as the gustiness of
290 wind might play an important role. In certain parts of the globe, such as Peru upwelling region, the South Pacific Ocean, Indian Ocean, Arabian Sea, Bay of Bengal, **Coastal areas of continents**, North Atlantic Ocean, Gulf of Alaska, and Southern Ocean, etc., the differences between the climatological estimated DMS of G18, W20, H22 can be **observed** (Paper: Part A). Hence, the uncertainty in total flux emission is dominated by uncertainty due to useawater DMS concentration in these areas **where the**
295 **differences are significant** (Fig.3). In other regions, **it** is dominated by uchoice in ucoefficient of uflux parametrization, such as the coastal area of Antarctica and the Arctic Ocean. uComparison of in situ and co-located estimated flux show uthat all the **estimations** overestimate the DMS flux below $20 \mu\text{mol m}^{-2} \text{d}^{-1}$ but underestimate fluxes larger than $20 \mu\text{mol m}^{-2} \text{d}^{-1}$. This suggests that emissions in current models overestimate the total sea-air DMS **flux but underestimate the higher range** when it can significantly impact new particle formation and growth.

Code availability

300 Codes for the analysis and figures are available on request.

Data availability



All the data used here are publicly available and links are provided in the manuscript.

Competing Interests

The authors declare that they have no conflict of interest.

305 Author Contributions

ASM conceptualized the study. SJ analyzed the data with help from SH. CM, MG, MY, TB and RS helped with the data, ideas and understanding of the study. SJ and ASM wrote the manuscript with the help of all the coauthors.

Acknowledgements

310 The Indian Institute of Tropical Meteorology is funded by the Ministry of Earth Sciences, Government of India. MG and RS acknowledge support from the European Research Council (ERC) under the European Union's Horizon 2020 research and innovation program (grant agreement #834162, SUMMIT Advanced Grant to RS), and the Spanish Government through grant GOOSE (PID2022_140872NB_I00) as well as the "Severo Ochoa Centre of Excellence" accreditation grant CEX2019-000928-S.

References

- 315 Andreae, M. O. and Crutzen, P. J.: Atmospheric aerosols: Biogeochemical sources and role in atmospheric chemistry, *Science* (80-.), 276, 1052–1058, 1997.
- Andreae, M. O. and Raemdonck, H.: Dimethylsulfide in the surface ocean and the marine atmosphere: A Global View, *Science* (80-.), 221, 744–747, 1983.
- Bhatti, Y. A., Revell, L. E., Schuddeboom, A. J., Mcdonald, A. J., Archibald, A. T., Williams, J., Venugopal, A. U., Hardacre, C., Behrens, E., and Bhatti, Y.: The sensitivity of Southern Ocean atmospheric dimethyl sulfide to modelled sources and emissions, 15181–15196, 2023.
- 320 Carpenter, L. J., Archer, S. D., and Beale, R.: Ocean-atmosphere trace gas exchange, *Chem. Soc. Rev.*, 41, 6473–6506, <https://doi.org/10.1039/c2cs35121h>, 2012.
- Cember, R.: Bomb radiocarbon in the Red Sea: A medium-scale gas exchange experiment, *J. Geophys. Res.*, 94, 2111, <https://doi.org/10.1029/JC094iC02p02111>, 1989.
- 325 Charlson, R. J., Lovelock, J. E., Andreae, M. O., and Warren, S. G.: Ocean phytoplankton, atmospheric sulfur, cloud albedo and climate, *Nature*, 326, 655–661, <https://doi.org/10.1029/2003GB002183>, 1987.
- Coale, K. H., Johnson, K. S., Fitzwater, S. E., Gordon, R. M., Tanner, S., Chavez, F. P., Ferioli, L., Sakamoto, C., Rogers, P., Millero, F., Steinberg, P., Nightingale, P., Cooper, D., Cochlan, W. P., Landry, M. R., Constantinou, J., Rollwagen, G.,
- 330 Trasvina, A., and Kudela, R.: A massive phytoplankton bloom induced by an ecosystem-scale iron fertilization experiment in



the equatorial Pacific Ocean, *Nature*, 383, 495–501, <https://doi.org/10.1038/383495a0>, 1996.

Dacey, J. W. H. and Wakeham, G.: HENRY'S LAW CONSTANTS FOR DIETHYLSULFIDE IN FRESHWATER AND SEAWATER, 11, 991–994, 1984.

335 Erickson, D. J.: A stability dependent theory for air-sea gas exchange, *J. Geophys. Res. Ocean.*, 98, 8471–8488, <https://doi.org/10.1029/93JC00039>, 1993.

Galí, M., Levasseur, M., Devred, E., Simó, R., and Babin, M.: Sea-surface dimethylsulfide (DMS) concentration from satellite data at global and regional scales, 15, 3497–3519, <https://doi.org/10.5194/bg-15-3497-2018>, 2018.

340 Goddijn-Murphy, L., Woolf, D. K., and Marandino, C.: Space-based retrievals of air-sea gas transfer velocities using altimeters: Calibration for dimethyl sulfide, *J. Geophys. Res. Ocean.*, 117, n/a-n/a, <https://doi.org/10.1029/2011JC007535>, 2012.

Ho, D. T., Law, C. S., Smith, M. J., Schlosser, P., Harvey, M., and Hill, P.: Measurements of air-sea gas exchange at high wind speeds in the Southern Ocean: Implications for global parameterizations, *Geophys. Res. Lett.*, 33, L16611, <https://doi.org/10.1029/2006GL026817>, 2006.

345 Hulswar, S., Simó, R., Galí, M., Bell, T. G., Lana, A., Inamdar, S., Halloran, P. R., Manville, G., and Mahajan, A. S.: Third revision of the global surface seawater dimethyl sulfide climatology (DMS-Rev3), *Earth Syst. Sci. Data*, 14, 2963–2987, <https://doi.org/10.5194/essd-14-2963-2022>, 2022.

Ishii, M., Shouji, A., Sugimoto, S., and Matsumoto, T.: Objective analyses of sea-surface temperature and marine meteorological variables for the 20th century using ICOADS and the Kobe Collection, *Int. J. Climatol.*, 25, 865–879, <https://doi.org/10.1002/joc.1169>, 2005.

350 Jahne, B., Münnich, K. O., and Siegenthaler, U.: Measurements of gas exchange and momentum transfer in a circular wind-water tunnel, 31, 321–329, <https://doi.org/10.3402/tellusa.v31i4.10440>, 1979.

Jähne, B., Münnich, K. O., and Siegenthaler, U.: Measurements of gas exchange and momentum transfer in a circular wind-water tunnel, *Tellus A Dyn. Meteorol. Oceanogr.*, 31, 321, <https://doi.org/10.3402/tellusa.v31i4.10440>, 1979.

355 Jähne, B., Huber, W., Dutzi, A., Wais, T., and Ilmberger, J.: Wind/Wave-Tunnel Experiment on the Schmidt Number — and Wave Field Dependence of Air/Water Gas Exchange, in: *Gas Transfer at Water Surfaces*, Springer Netherlands, Dordrecht, 303–309, https://doi.org/10.1007/978-94-017-1660-4_28, 1984.

Kalnay, E., Kanamitsu, M., Kistler, R., Collins, W., Deaven, D., and Gandin, L.: The NCEP / NCAR 40-Year Reanalysis Project, *Bull. Am. Meteorol. Soc.*, 437–472, [https://doi.org/10.1175/1520-0477\(1996\)077<0437:TNYRP>2.0.CO;2](https://doi.org/10.1175/1520-0477(1996)077<0437:TNYRP>2.0.CO;2), 1996.

360 Kettle, A. J. and Andreae, M. O.: Flux of dimethylsulfide from the oceans: A comparison of updated data sets and flux models, *J. Geophys. Res. Atmos.*, 105, 26793–26808, <https://doi.org/10.1029/2000JD900252>, 2000.

Lana, A., Bell, T. G., Simó, R., Vallina, S. M., Ballabrera-Poy, J., Kettle, A. J., Dachs, J., Bopp, L., Saltzman, E. S., Stefels, J., Johnson, J. E., and Liss, P. S.: An updated climatology of surface dimethylsulfide concentrations and emission fluxes in the global ocean, *Global Biogeochem. Cycles*, 25, 1–17, <https://doi.org/10.1029/2010GB003850>, 2011.

Liss, P. S. and Merlivat, L.: Air-Sea Gas Exchange Rates: Introduction and Synthesis, in: *The Role of Air-Sea Exchange in*



- 365 Geochemical Cycling, vol. 1983, Springer Netherlands, Dordrecht, 113–127, https://doi.org/10.1007/978-94-009-4738-2_5, 1986.
- Marandino, C. A., De Bruyn, W. J., Miller, S. D., and Saltzman, E. S.: Open ocean DMS air/sea fluxes over the eastern South Pacific Ocean, *Atmos. Chem. Phys.*, 9, 345–356, <https://doi.org/10.5194/acp-9-345-2009>, 2009.
- McNabb, B. J. and Tortell, P. D.: Improved prediction of dimethyl sulfide (DMS) distributions in the northeast subarctic Pacific using machine-learning algorithms, 19, 1705–1721, <https://doi.org/10.5194/bg-19-1705-2022>, 2022.
- 370 Monahan, E. C. and Spillane, M. C.: The Role of Oceanic Whitecaps in Air-Sea Gas Exchange, in: *Gas Transfer at Water Surfaces*, Springer Netherlands, Dordrecht, 495–503, https://doi.org/10.1007/978-94-017-1660-4_45, 1984.
- Nightingale, D., Malin, G., Law, C. S., Watson, J., Liss, S., and Liddicoat, I.: In situ evaluation of air-sea gas exchange parameterizations using novel conservative and volatile tracers., *Global Biogeochem. Cycles*, 14, 373–387, <https://doi.org/10.1029/1999GB900091>, 2000.
- 375 Omori, Y., Tanimoto, H., Inomata, S., Ikeda, K., Iwata, T., Kameyama, S., Uematsu, M., Gamo, T., Ogawa, H., and Furuya, K.: Sea-to-air flux of dimethyl sulfide in the South and North Pacific Ocean as measured by proton transfer reaction-mass spectrometry coupled with the gradient flux technique, *J. Geophys. Res.*, 122, 7216–7231, <https://doi.org/10.1002/2017JD026527>, 2017.
- 380 Saltzman, E. S., King, D. B., Holmen, K., and Leck, C.: Experimental determination of the diffusion coefficient of dimethylsulfide in water, *J. Geophys. Res.*, 98, 16481, <https://doi.org/10.1029/93JC01858>, 1993.
- Simó, R.: Production of atmospheric sulfur by oceanic plankton : biogeochemical , ecological and evolutionary links, *Trends Ecol. Evol.*, 16, 287–294, 2001.
- Simó, R. and Dachs, J.: Global ocean emission of dimethylsulfide predicted from biogeophysical data, *Global Biogeochem. Cycles*, 16, 26-1-26–10, <https://doi.org/10.1029/2001gb001829>, 2002.
- 385 Wang, W. L., Song, G., Primeau, F., Saltzman, E. S., Bell, T. G., and Moore, K. K.: Global ocean dimethyl sulfide climatology estimated from observations and an artificial neural network, 17, 5335–5354, <https://doi.org/10.5194/bg-17-5335-2020>, 2020.
- Wanninkhof, R.: Relationship between wind speed and gas exchange over the ocean, *J. Geophys. Res.*, 97, 7373–7382, <https://doi.org/10.1029/92JC00188>, 1992.
- 390 Wanninkhof, R.: Relationship between wind speed and gas exchange over the ocean revisited, *Limnol. Oceanogr. Methods*, 12, 351–362, <https://doi.org/10.4319/lom.2014.12.351>, 2014.
- Wanninkhof, R., Asher, W., Weppernig, R., Chen, H., Schlosser, P., Langdon, C., and Sambrotto, R.: Gas transfer experiment on Georges Bank using two volatile deliberate tracers, *J. Geophys. Res.*, 98, 20237, <https://doi.org/10.1029/93JC01844>, 1993.
- Wanninkhof, R., Hitchcock, G., Wiseman, W. J., Vargo, G., Ortner, P. B., Asher, W., Ho, D. T., Schlosser, P., Dickson, M.-L., Masserini, R., Fanning, K., and Zhang, J.-Z.: Gas exchange, dispersion, and biological productivity on the West Florida Shelf: Results from a Lagrangian Tracer Study, *Geophys. Res. Lett.*, 24, 1767–1770, <https://doi.org/10.1029/97GL01757>, 1997.
- 395 Watson, A. J., Upstill-Goddard, R. C., and Liss, P. S.: Air–sea gas exchange in rough and stormy seas measured by a dual-



tracer technique, *Nature*, 349, 145–147, <https://doi.org/10.1038/349145a0>, 1991.

400 Yan, S. B., Li, X. J., Xu, F., Zhang, H. H., Wang, J., Zhang, Y., Yang, G. P., Zhuang, G. C., and Chen, Z.: High-resolution distribution and emission of dimethyl sulfide and its relationship with pCO₂ in the Northwest Pacific Ocean, *Front. Mar. Sci.*, 10, 1–12, <https://doi.org/10.3389/fmars.2023.1074474>, 2023.

Zhang, M., Marandino, C. A., Yan, J., Wu, Y., Park, K., Sun, H., Gao, Z., and Xu, S.: Unravelling Surface Seawater DMS Concentration and Sea-To-Air Flux Changes After Sea Ice Retreat in the Western Arctic Ocean, *Global Biogeochem. Cycles*,

405 35, 1–15, <https://doi.org/10.1029/2020GB006796>, 2021.

Zhao, D., Toba, Y., Suzuki, Y., and Komori, S.: Effect of wind waves on air-sea gas exchange: proposal of an overall CO₂ transfer velocity formula as a function of breaking-wave parameter, *Tellus B Chem. Phys. Meteorol.*, 55, 478–487, <https://doi.org/10.3402/tellusb.v55i2.16747>, 2003.

410 Tables :

Table 1. Area Weighted Global mean flux standard deviation for each month and annually due to σ_{DMS} , σ_k and σ_{wind} . Also, DMS_{Sulfur} emissions for each month and annually from the areas with $\sigma_{DMS} > \sigma_k$ and the area $\sigma_{DMS} < \sigma_k$ and the total emission across the globe is computed using the N00b flux parameterization and H22 DMS climatology.

Month	Area Weighted Global Mean Flux std. due to σ_{DMS} ($\mu\text{mol m}^{-2} \text{d}^{-1}$)	Area Weighted Global Mean Flux std. due to σ_k ($\mu\text{mol m}^{-2} \text{d}^{-1}$)	Area Weighted Global Mean Flux std. due to σ_{wind} ($\mu\text{mol m}^{-2} \text{d}^{-1}$)	DMS _{Sulfur} emissions where $\sigma_{DMS} > \sigma_k$ (Tg)	DMS _{Sulfur} emissions where $\sigma_{DMS} < \sigma_k$ (Tg)	Total DMS _{Sulfur} emissions (Tg)
January	1.85	1.69	0.16	1.47	0.85	2.33
February	1.42	1.29	0.13	1.07	0.68	1.74
March	1.52	1.28	0.13	1.54	0.50	2.04
April	1.07	0.99	0.10	0.98	0.52	1.50
May	1.31	1.09	0.11	1.11	0.51	1.62
June	1.51	1.09	0.11	1.24	0.49	1.73
July	1.39	1.09	0.12	1.29	0.52	1.81
August	1.41	1.08	0.12	1.42	0.47	1.89
September	1.04	0.83	0.09	1.09	0.41	1.50
October	1.08	0.94	0.10	0.97	0.63	1.60
November	1.79	1.47	0.14	1.36	0.60	1.96
December	1.82	1.70	0.16	1.40	0.90	2.30
Annual	1.44	1.21	0.12	17.16	4.93	22.08



415 **Figures :**

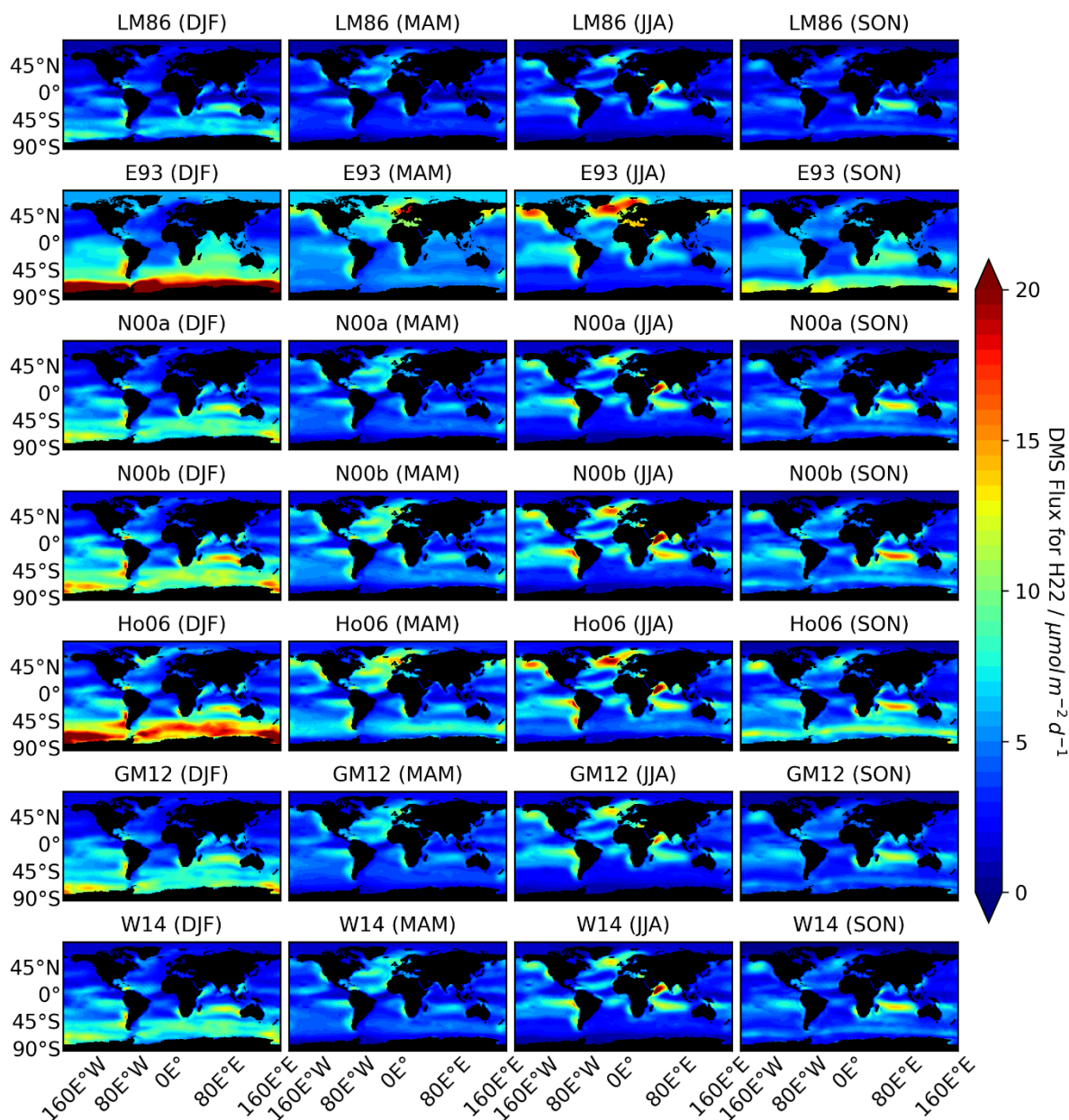


Figure 1: DMS fluxes estimated using the seven parameterizations for different seasons using the H₂₂ climatology. The geographical pattern is similar in all the estimates, although the absolute values differ according to the parameterization chosen. In JJA, maximum flux of 33.75 $\mu\text{mol m}^{-2} \text{d}^{-1}$ is observed in Indian ocean near Somalia with N00b. In DJF, maximum flux obtained 45.82 $\mu\text{mol m}^{-2} \text{d}^{-1}$ in Weddell Sea region with E93.

420

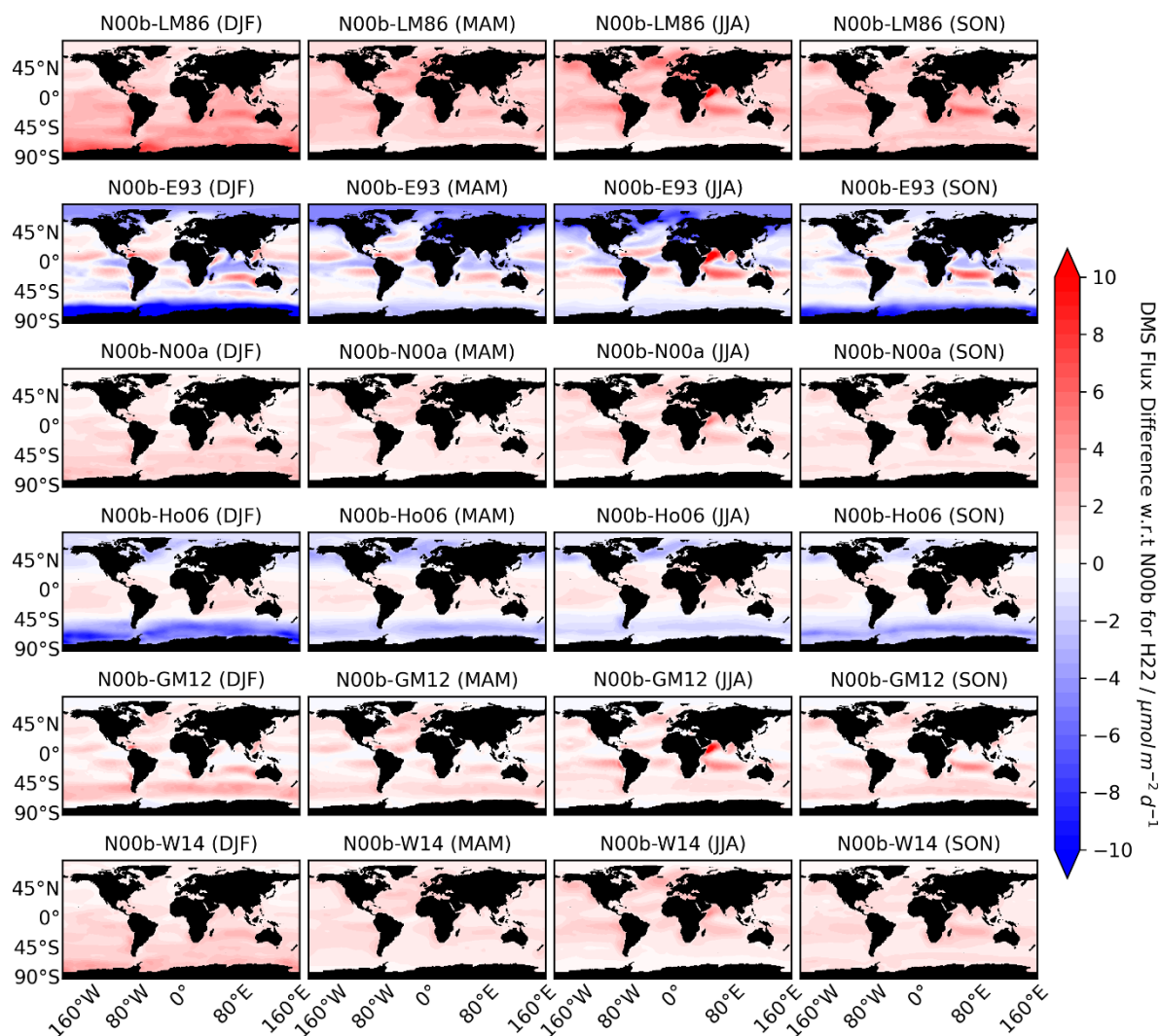


Figure 2: Differences between the DMS fluxes estimated using H22 with the N00b parameterization and the other seven parameters. For all the seasons, N00b-LM86 shows a positive difference, while the other parameterizations (E93, Ho06) show negative differences in the Southern Ocean and Arctic region, although some positive differences are also present in E93 and Ho06 in mid latitude regions. GM12, W14 and N00a show small positive differences with N00b while N00b-LM86 shows significant large positive difference.

425

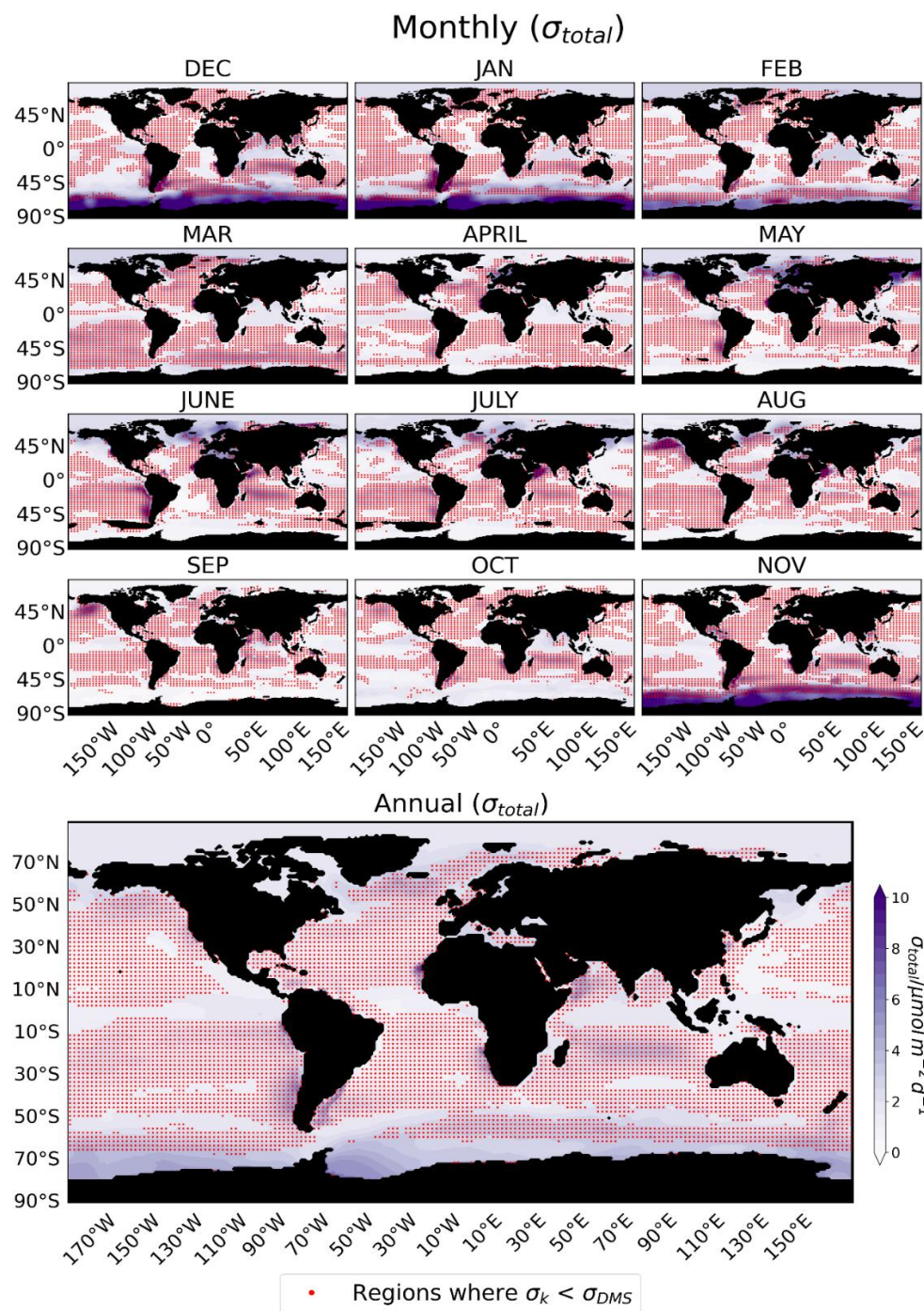


Figure 3: An estimate of the total variation (σ_{total}) in the flux emission, which is shown as a background map and is obtained from the standard deviations in the seawater DMS concentrations (σ_{DMS}), standard deviations in the coefficients of parametrizations (σ_k) and variation due to wind speed (σ_{wind}). σ_{wind} has a small contribution compared to σ_{DMS} and σ_k (Table 1). The regions where seawater DMS concentrations drive the uncertainty are indicated by red dots ($\sigma_{DMS} > \sigma_k$), while in the other areas (no red dots), it is driven by the variation due to the choice of the flux parameterization ($\sigma_{DMS} < \sigma_k$).

430

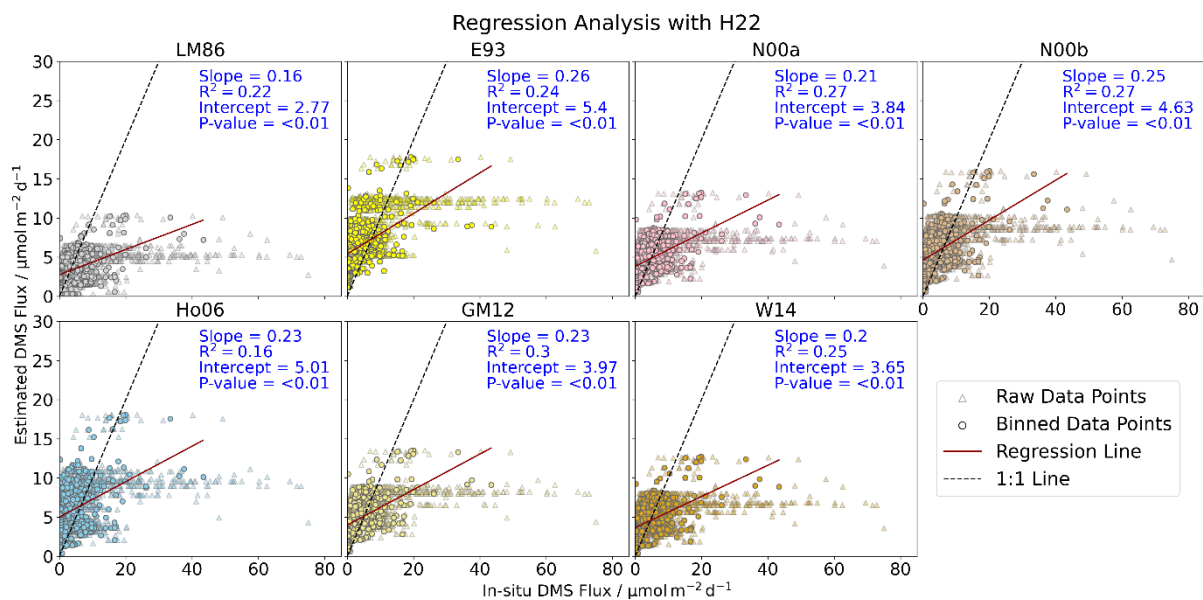


Figure 4: Comparison of in situ and estimated DMS fluxes (using H22) with the different parameterizations. Here, the regression analysis is done with binned in situ data at $1^\circ \times 1^\circ$ resolution, as the flux climatologies are also at the same resolution. Analysis shows that flux calculations result in **higher fluxes than observations at low levels** ($< 20 \mu\text{mol m}^{-2} \text{d}^{-1}$) and **lower fluxes than observations at higher levels** ($> 20 \mu\text{mol m}^{-2} \text{d}^{-1}$), which indicates that flux parametrization methods **fail to represent high flux values**. The black dash line is the 1:1 representation between in situ and the estimated DMS flux points, and the dark red line is the regression line. A list of the in situ observations used for the comparison is given in Table S1

435